

UC Davis

UC Davis Previously Published Works

Title

Spatial Sensing Using Electrical Impedance Tomography

Permalink

<https://escholarship.org/uc/item/0m12m1vn>

Journal

IEEE Sensors Journal, 13(6)

ISSN

1530-437X

Authors

Loyola, BR
Saponara, VL
Loh, KJ
[et al.](#)

Publication Date

2013-05-23

DOI

10.1109/jsen.2013.2253456

Peer reviewed

Spatial Sensing Using Electrical Impedance Tomography

Bryan R. Loyola, Valeria La Saponara, Kenneth J. Loh, *Member, IEEE*, Timothy M. Briggs, Gregory O'Bryan, and Jack L. Skinner, *Member, IEEE*

Abstract—The need for structural health monitoring has become critical, due to aging infrastructures, legacy airplanes, and continuous development of new structural technologies. With updated structural design comes the need for new structural health monitoring paradigms that can sense the presence, location, and severity with a single measurement. This paper focuses on the first step of this paradigm, consisting of applying a sprayed conductive carbon nanotube-polymer film upon glass fiber-reinforced polymer composite substrates. Electrical impedance tomography is performed to measure changes in conductivity within the conductive films due to damage. Simulated damage is a method for validation of this approach. Finally, electrical impedance tomography measurements are taken while the conductive films are subjected to tensile and compressive strain states. This demonstrates the ability of electrical impedance tomography for not only damage detection, but active structural monitoring as well. This study acts as a first step towards moving the structural health monitoring paradigm towards large-scale deployable spatial sensing.

Index Terms— Carbon Nanotubes, Electrical Impedance Tomography, Nanocomposites, Structural Health Monitoring

I. INTRODUCTION

Engineers are entrusted with ensuring the safety and longevity of a variety of structures in use today, which stem from the numerous engineering advances in the 20th century. These accomplishments include the U.S Interstate highway system, high-rise buildings, and propeller and jet-powered aircraft. As important as these technological accomplishments are, this vital infrastructure is deteriorating as indicated by the

Manuscript received DATE. This research is supported by the National Science Foundation (NSF) under Grant No. CAREER CMMI-0642814 and Grant No. 1200521. Additional support has also been provided by the University of California, Center for Information Technology Research in the Interest of Society (CITRIS), the National Institute of Nano Engineering at Sandia National Laboratories, and the UC Davis Dissertation Year Fellowship.

B. R. Loyola, T. M. Briggs, and G. O'Bryan are with Sandia National Laboratories, Livermore, CA 94550, USA (e-mail: brloyol@sandia.gov).

V. La Saponara is with the Mechanical and Aerospace Engineering Department, University of California, Davis, CA 95616, USA (e-mail: vlasaponara@ucdavis.edu).

K. J. Loh is with the Civil and Environmental Engineering Department, University of California, Davis, CA 95616, USA (e-mail: kjloh@ucdavis.edu).

J. L. Skinner is with the General Engineering Department, Montana Tech of the University of Montana, Butte, MT 59701, USA (email: jskinner@mtech.edu).

2009 ASCE report card's overall 'C' rating for safety of the bridges in the United States, while stating that the average bridge is 43 years old of a 50 year life span [1]. Another recent example includes a 2008 incident involving Southwest Flight 812, which experienced a rapid depressurization of the cabin due to a rupture in the fuselage. This structural failure was attributed to fatigue cracking near riveted lap-joints [2]. Monitoring is also necessary for next-generation structures, such as fiber-reinforced composite-based aircraft, radar-evading naval vessels, and super-span suspension bridges among others, for any unexpected modalities of damage to develop. In 2005, two Airbus A-300 series aircraft had incidents where the fiber-reinforced composite skin of the aircraft rudders debonded. In one case, the debond degraded the structural integrity of the rudder to the point where the rudder sheared-off of the aircraft in flight [3]. In another case involving a new structural design using traditional metals, numerous cracks have developed on the U.S. Navy's Ticonderoga cruisers [4] and the Littoral Combat Ship U.S.S. Freedom [5], which have traditional steel hulls with aluminum superstructures. Many of the cracks have developed at the bi-metal interfaces, both above and below the water line. With the sheer magnitude of the work involved to monitor our increasing infrastructure, low-cost and automated systems will have to be implemented to aid in this colossal task.

To confront these problems, numerous research groups have developed means to implement a variety of sensing methodologies within real structures. One of these methods involved the implementation of a foil-based strain gauge network, which monitors for changes in the strain field of the structures. Some examples of this work have been applied to wind turbines [6], rail structures [7], and aircraft [8]. Other researchers have looked at the implementation of strain gauge networks with wireless systems [9]. Other groups have focused on using optical fiber Bragg gratings to measure strain and temperature in a wide array of structures, such as aircraft [10, 11], U.S. Navy fast patrol boats [12], spacecraft [13], rocket motors [14], and bridges [15-17]. The foil-based strain gauges and fiber Bragg gratings are point-based sensors that measure the strain and temperature at the point of application. To get a global view of the structure's health, interpolation and other data analysis methods are employed to determine structural degradation or damage development. Many researchers have chosen to implement networks of piezoelectric transducers and receivers, to propagate guided

waves through the structure to detect potential damage. A few examples include implementation in aircraft [18], naval structures [19], civil infrastructure [20, 21], rail bridges [22], and spacecraft [23, 24]. Although acoustic-/ultrasonic-based approaches are typically much better at detecting damage away from sensor placement, there are still some issues with their effectiveness in structures with multiple interfaces, poor transmission properties (*e.g.*, structural foams), and damage detection when collocated with the damaged area. These systems leverage already proven and off-the-shelf technologies that have been used for a number of years but still have issues that need to be solved or supplemented with another methodology to ensure complete and robust monitoring for a given structure.

In recent years, a newer field has emerged by developing a structural health monitoring methodology based on measuring the change in the electrical properties inherent to a structure or an applied conductive material to measure strain and detect damage within the structure. The increase in the use of carbon fiber-reinforced polymers (CFRPs) has allowed researchers to monitor for different aspects of structural health, namely, by measuring the change in time-domain or direct current (DC)-based electrical resistance before, during, and after a loading event. Several groups have successfully detected strain [25-29], delamination [30-32], and traverse cracking [25, 33] in CFRP. For materials that are electrically nonconductive such as glass fiber reinforced polymers (GFRPs), or materials that are too conductive to have a resistance change above the noise threshold, thin films based on carbon nanotubes (CNTs) have been developed for application to the surface or embedded within materials with a layered construction like fiber-reinforced composites. These films are capable of sensing strain [34-39], cracks [40, 41], temperature [42-44], humidity [45-47], and changes in pH [48]. All of these measurements were done using 2- or 4-point probe resistance measurements, where the change in electrical properties is measured between the inner electrodes. If strain or damage is incurred within the gauge section of the sensor, the effect is registered by the measurement, but the location of damage cannot be determined. Although multiple measurements taken in a hash pattern can resolve this problem, this approach still leads to poor resolution and necessitates a large number of measurements.

A method called electrical impedance tomography (EIT) has been a focus of medical and geophysical research for the past 30 years but has been relatively overlooked by the SHM community until very recently. EIT allows for the reconstruction of the spatially distributed conductivity within a sensing area bounded by a set of electrodes. However, the reconstruction of this distributed conductivity is ill-posed, and a solution has only been available since Calderon's paper in 1980 [49]. Once Calderon's strategy for conductivity reconstruction was discovered, numerous research groups have improved on this strategy by developing linear [50-54] and non-linear [51, 54-57] reconstruction algorithms depending on the topology of the conductivity distribution. Also, these reconstructions can be performed for absolute or

differential imaging, where the actual or change in conductivity can be determined, respectively. The EIT community has developed a MATLAB script suite called Electrical Impedance Tomography and Diffuse Optical Tomography Reconstruction Software (EIDORS) [58]. Despite this progress, only a few groups have released research relating to applying EIT to applied conductive films for SHM purposes. Lazarovitch et al. [59] demonstrated the ability to monitor changes in conductivity using a carbon film, with potential applications to impact-damage monitoring. Pyo et al. [60], Hou et al. [61], and Loh et al. [62] have published on the use of EIT for applied monitoring using a layer-by-layer CNT-polyelectrolyte thin films for strain, impact, pH, and corrosion detection. However, these studies involved sensitive thin films that cannot be easily or cheaply scaled up for large engineering structures.

To bring EIT closer to a large-scale SHM methodology, an easily deployable conductive medium needs to be developed and shown to work in conjunction with EIT for spatially distributed sensing to changes in conductivity. In this study, these very accomplishments are demonstrated through the development of a multi-walled carbon nanotube (MWNT)-polyvinylidene fluoride (PVDF) latex-based film that can be spray-deposited on surfaces of unlimited size. Furthermore, these films are used as a sensitive conductive medium for performing EIT measurements, and thus, monitor for changes in conductivity due to applied strain and simulated damage. The purpose of this work is to show that EIT merits serious attention as a field deployable SHM methodology.

II. ELECTRICAL IMPEDANCE TOMOGRAPHY

EIT is a soft-field tomographic method that allows for the reconstruction of the 2D or 3D spatially distributed conductivity of a conductive medium that is bounded by electrodes. A typical measurement entails propagating a current between two electrodes and measuring the corresponding differential voltage at the remaining boundary electrodes. Specifically, a current is injected into one electrode and another electrode is connected with ground. These measurements are performed for a set of current injections, called a current injection pattern. The corresponding boundary voltage measurements are correlated to the spatially distributed conductivity via Laplace's equation:

$$\nabla \cdot (\sigma \nabla u) = 0 \quad (1)$$

Typically, the forward problem is solved where the conductivity distribution (σ) is known and the voltage distribution (u) across the conductive medium is solved. However, the purpose of EIT is to solve the inverse problem, or the exact opposite of this case. Inevitably, the forward problem is solved in some form while performing the inverse problem calculation. As analytical solutions are not typically available for most geometries, a numerical approach is taken using the finite element method (FEM). The weak formulation of Laplace's equation is developed, which results in the

following:

$$\iint_{\Omega} \sigma_{\Omega} \nabla \phi \nabla u dx dy = 0 \quad (2)$$

In the case of this study, a 2D approach is taken using triangular elements, where (2) is performed over the area of each of these elements (Ω). In this FEM formulation, piecewise linear shape functions (ϕ) are used to account for the voltage at each node. To properly model the effects of electrode contact resistance, the complete electrode model [63] is applied, where:

$$\int_{E_i} \sigma \frac{\partial u}{\partial \nu} ds = I_i \quad (3)$$

$$u + z_i \sigma \frac{\partial u}{\partial \nu} = V_i \quad (4)$$

At the current injection electrode (l), the boundary conduction problem is governed by (3), where the current is injected normal (ν) to the boundary at the electrode at a magnitude of I_l . Due to the electrode contact resistance (z_l), a voltage drop occurs between the electrode and the conductive medium. The voltage drop across each electrode due to contact resistance is accounted for by (4), where the corresponding mesh voltage is u , and V_l is the electrode voltage. In addition, the grounded electrode boundary condition, as part of each current injection pair, is implemented with (4), where V_l is set to zero. The FEM discretization of (1) with the corresponding boundary conditions (3) and (4) is solved in matrix form for each current injection, for the corresponding voltage distribution and the boundary electrode boundaries simultaneously [56].

To perform the EIT conductivity reconstruction, the absolute or differential distributed conductivity image can be reconstructed. Absolute imaging uses one set of electrode voltage measurement to reconstruct the actual conductivity within the sensing area of the measurement. Differential imaging uses two sets of EIT voltage measurements in time to reconstruct the change in the conductivity reconstruction. Previous work has shown that differential imaging is more stable [64] and, for the purposes of SHM, is more applicable than absolute imaging, because changes in conductivity are typically indicative of the onset of damage.

In this work, a normalized differential imaging reconstruction method called Maximum a Posteriori (MAP) is discussed, which was developed by Adler and Guardo [50]. In general, MAP is a one-step linear reconstruction method that requires relative changes in conductivity to be less than a $\pm 100\%$ change in conductivity, for the reconstruction to be accurate. The advantage of using this method is a lower dependence of the reconstruction on the knowledge of the exact boundary electrode contact resistances and the current used for the injections. To perform this type of imaging, two sets of boundary voltage measurements are required, where the difference of the measurements is divided by the initial

voltage measurements for normalized differential voltage values. These values are used in conjunction with the MAP reconstruction equation in (5), to determine the normalized change in conductivity:

$$\frac{\Delta \sigma}{\sigma_0} = \left(H^T W H + \lambda R \right)^{-1} H^T W \left(\frac{\Delta V}{V_0} \right) \quad (5)$$

The matrix H is the sensitivity matrix that correlates the normalized change in boundary electrode voltage to a change in the spatial normalized change in the conductivity. The calculation of the sensitivity matrix is fully outlined by Adler and Guardo [50]. To incorporate the effect of Gaussian white noise in the voltage measurements, the variance of these measurements are used in the W matrix, where:

$$W_{i,i} = \frac{1}{\alpha_i}, \quad W_{i,j} = 0 \text{ for } i \neq j \quad (6)$$

The variable α_i is the variance of the corresponding boundary voltage measurement i . Due to the ill-posed nature of the reconstruction, regularization is implemented for stabilization of the calculation, in the form of a regularization matrix R and a regularization hyperparameter λ . The regularization matrix typically implements some sort of smoothing in the reconstruction, using approaches such as Tikhonov's [65], NOSER [52], discrete Laplacian filtering [66], and Gaussian high-pass filtering [50]. In this study, the Gaussian high-pass filter regularization matrix is used due to the proven efficacy in conjunction with the MAP algorithm. To determine the scalar value of the regularization hyperparameter, the noise figure (NF) metric is implemented. First discussed by Adler and Guardo [50] and refined by Graham and Adler [64], the NF metric mandates that the signal-to-noise ratio of the reconstructed normalized differential conductivity distribution be a specified multiple of the signal-to-noise ratio of the normalized differential voltage measurements used for the reconstruction. This calculation is performed for a representative system for which future reconstructions will be performed with a small contrast of 50 % in the center of the sensing area. This contrast can be negative to positive, whichever best relates to the sensing tests conducted. In this study, an NF of 1 is used, which is selected to ensure that the reconstruction is not under- or over-regularized. Upon the determination of the regularization hyperparameter, the MAP linear reconstruction equation is fully determined, and the reconstruction for the sensing system defined by its components can now be conducted.

III. EXPERIMENTAL METHODS

In order for EIT to be used for SHM purposes with non-conductive materials, a conductive material must be deposited, as is the case with GFRP composites. The present work utilized a conductive MWNT-PVDF latex-based film that was

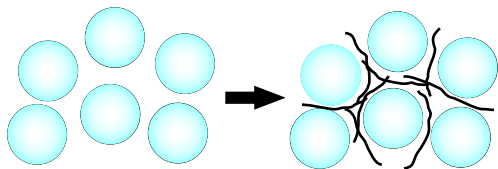


Fig. 1 Representation of the segregated MWNT network within the PVDF latex solution prior to film formation.

spray-deposited on substrates on the order of hundreds of square-centimeters. The capability of the EIT method was then tested for sensitivity to complex shaped conductivity distributions and for validation of distributed sensing. Finally, applied films on GFRP specimens were characterized for their strain sensitivity in conjunction with the EIT methodology.

A. MWNT-PVDF Latex Coating

The MWNT-PVDF films were based on a two-part system that allowed for shelf-stable solutions. When combined, it led to a robust, conductive film. The first part of the solution contained the polymer matrix that was obtained commercially as a latex solution of 150 nm particles of PVDF (Arkema). This solution was adjusted with water to ensure that the resulting mixed paint had a specific weight percentage of solids to water. The other solution contained the conductive MWNTs (SWeNT) that were stably suspended in water using poly(sodium 4-styrenesulfonate) (PSS) (~1 MW, Sigma-Aldrich) and the addition of the polar solvent N-methyl-2-pyrrolidone (NMP) (Sigma-Aldrich). NMP acted as a coalescing agent of the PVDF, which facilitated the forming of the film when used in an amount of 3 wt.% compared to the total mass of the PVDF particles. The amount of MWNTs was determined by a specified weight percentage of MWNTs in the fully dried film. In this study, 5 wt.% of MWNTs was used.

The conductive solution was formed starting with a 2 wt.% solution of PSS that was tip-sonicated in an ice-bath for 10 min or until completely dissolved. NMP and powder-form MWNTs were then added to the PSS solution, followed by 30 min of tip-sonication. During tip-sonication, the PSS polymer wrapped [67] the MWNTs to ensure an enduring dispersion and suspension, while the NMP also acted as a dispersing agent for MWNTs [68]. The PVDF latex solution was produced by combining the PVDF latex solution and an appropriate amount of DI water diluent to make a resulting combined paint that is 13 wt.% solid content, including the PVDF and the MWNTs.

To produce the final paint solution, the conductive ink and the PVDF solution were combined and thoroughly mixed. The resulting paint started to immediately thicken due to shear thickening by the MWNTs and the onset of coalescence from the NMP. This mixing created a segregated network of the MWNTs between the PVDF particles, as illustrated in Fig. 1. At this point, the conductive paint was sprayed onto a

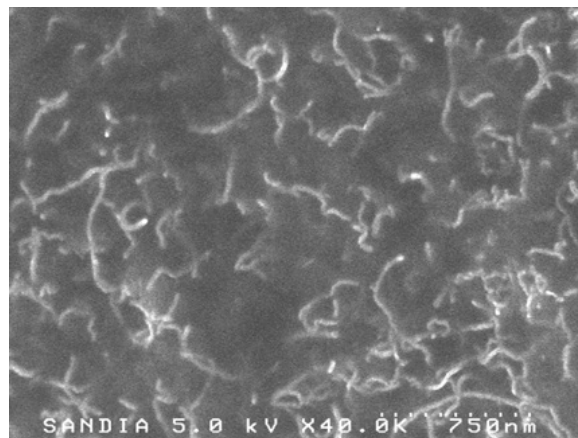


Fig. 2 Scanning electron microscope image of a cleaved surface of the MWNT-PVDF film.

substrate using an airbrush. Once sprayed, the paint rapidly began to dry due to evaporation. The painted specimens were placed in a 60 °C oven for 10 min, to fully evaporate the water. As the water evaporated, the NMP fully coalesced the PVDF particles, locking in the MWNT network. The resulting film and representative MWNT network is shown in the scanning electron microscope (SEM) image in Fig 2. The resulting sheet resistance of these films was on average 817.9 Ω per square with a standard deviation of 117.5 Ω per square.

B. EIT Measurements

In order to conduct the EIT measurements, current needs to be injected into one electrode, another electrode needs to be set to ground, and the remaining electrodes need to be measured for the corresponding voltage response. To do this, each electrode around a sensing skin was connected to a Agilent 34923A matrix switch attached to an Agilent 34980A data acquisition unit. A Keithley 6221 alternating current (AC) and DC current source was used in conjunction with the analog inputs of the 34980A to provide the current input and ground. The current injection pattern for all of the EIT measurements in this study were between two electrodes directly across from one another, as shown in Fig. 3, where each blue line represents one injection-ground pair. A full EIT measurement consisted of the boundary voltage measurements corresponding to subsequent application of these pairs. To prevent voltage measurements that were affected by electrode contact resistance, voltage measurements involving the injecting or grounded electrodes were not included in measurements.

C. EIT Validation

To validate the responses from the MAP reconstruction algorithm, several conductivity patterns were spray-deposited with the airbrush using masked patterns onto pre-cured GFRP substrates. The GFRP substrates were prepared with a 100 grit diamond abrasion pad and cleaned with isopropanol and then

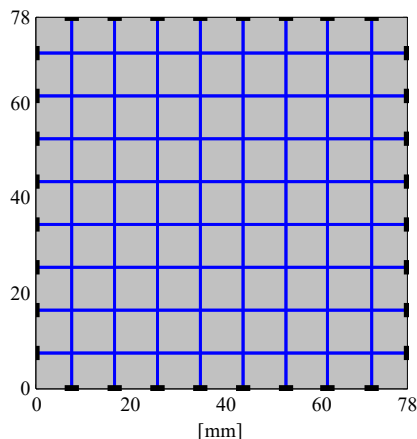


Fig. 3 Current injection pattern used in this study. The blue lines indicate generalized current path.

acetone. The masks for the electrodes, sensing area, and conductivity patterns were cut from sheets of polyester, using a CNC laser cutter. Specifically, the masked area included eight 3 mm square electrode pads extended from each edge of the 78×78 mm² sensing area, as shown in Fig. 4. The electrodes were placed 6 mm apart from each other. These electrodes pads facilitated easier placement of the electrodes during specimen preparation. The masks were applied to the substrates using double-backed masking tape. All of the substrates contained conductivity pattern masks except for one substrate. This homogeneous conductivity pattern was used as the baseline measurement for the normalized differential imaging. All of the substrates were lined up, and the MWNT-PVDF paint was spray-deposited on all of the substrates with continuous passes to yield a uniform coating across test specimens. After 50% of the paint was spray-deposited, all the conductivity pattern masks were removed, and the remaining 50% paint was applied. The specimens were then dried in a 60 °C oven for 10 min. After the film coalesced, 30 AWG wires were attached to each electrode pad using colloidal silver paint (Ted Pella). As can be seen in Fig. 4, this specimen had been masked with a 6 mm wide cross that is 54 mm long in the vertical and horizontal directions.

EIT measurements were taken for each specimen using a DC current injection magnitude of 100 μA. After the EIT measurements were completed, grids of 6 mm by 6 mm squares were drawn on each specimen (as shown in Fig. 4), and four-point probe resistance measurements were taken in each square. Using the resistance values, the conductivity distribution for each specimen was measured, and normalized difference values were calculated for each specimen with respect to the homogeneous MWNT-PVDF film. These measured conductivity distributions served as the validation for the EIT reconstructions.

D. MWNT-PVDF Piezoresistivity Characterization

Prior to characterizing the strain sensitivity of the MWNT-PVDF with EIT, the strain sensitivity of the films was

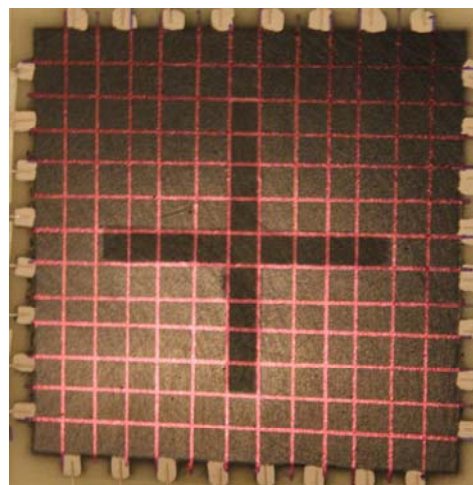


Fig. 4 EIT validation specimen with a 6 mm-wide cross contrast in the center. The lines indicate the grid where four-point probe resistance measurements were taken.

characterized using two-point probe resistance measurements as a point of comparison. MWNT-PVDF thin films were formulated with 3 wt.% MWNTs and spray-deposited on cured GFRP substrates. These substrates were manufactured using a hand-layup process, where a single layer of quasi-unidirectional glass fiber weave (type 7715, Applied Vehicle Technology) was infused with a two-part epoxy (125/237, Pro-Set Inc.). The composite was cured for 15 h at 27 °C and then for 8 h at 80 °C. Once the deposited films coalesced, the substrates were cut into 3×75 mm² strips with the 0° in the longitudinal direction. This followed the 1:11 width-to-length ratio recommended by the ASTM D 3039 standard for tensile testing composites [69]. To create electrical connections to the specimens, two 30 AWG wires were attached to the surface of the film, spaced 28 mm apart, using conductive colloidal silver paint. While loading these specimens in tension, serrated wedge-type grips were used to transfer the load to the specimens. To protect the specimens from the grips, G-10 GFRP tabs were bonded using aircraft-grade epoxy (Hysol 903, Henkel Corp.), so as to create a 25 mm gauge length.

To measure the change in the two-point resistance measurements, each specimen was connected to an Agilent 34401A digital multimeter for DC resistance measurements. A load frame (150R, TestResources Inc.) was used to place the specimens in tension. The displacement of the load frame was verified using a laser extensometer (Microtrak II, MTI Instruments). To allow for the resistance measurements to be taken at prescribed strain values, a stepped-displacement profile was used. For a higher resolution at lower-strain values, the load frame was paused for 60 s every 1,000 με from 0 to 10,000 με and every 5,000 με thereafter until failure. This strain profile allowed for characterizing the full strain response of the DC resistance properties. Negligible relaxation was observed during the pauses.

E. Four-point Flexure Test Procedure

In order to characterize the ability of the EIT reconstruction



Fig. 5 Four-point bending specimen in flexure fixture.

to capture the change in conductivity due to applied tensile and compression strains, an $18 \times 18 \text{ mm}^2$ sensing area was subjected to these strains, using four-point flexure tests. This test method allowed the specimens to be subjected to constant tensile and compression strains throughout the mid-span, below or above the neutral axis, respectively. The GFRP substrates were manufactured using a vacuum assisted resin transfer molding (VARTM) process, where unidirectional glass fiber mats (E-LR 0908, Vectorply) were infused with a two-part epoxy resin system (117LV/237, Pro-Set Inc.). The stacking sequence for these panels was $[0^\circ]_6$, and primary loading was along this principal axis. The infused panels were cured for 15 h at 27°C and then for 8 h at 80°C . Once cured, the specimens were cut into $25 \times 127 \text{ mm}^2$ specimens with the 0° fibers oriented in the longitudinal direction of the cut specimens. An $18 \times 18 \text{ mm}^2$ region, with 2 mm square electrodes spaced 2 mm apart, were masked on the center of each specimen and sprayed with the MWNT-PVDF film. The electrodes were applied and attached to 30 AWG wire wrap using a silver-loaded epoxy (Hysol TRA-DUCT 2902, Henkel).

The ASTM D 7264 standard was consulted for the four-point flexural tests. The outer supports of the flexural fixture were placed 101.6 mm apart, while the inner supports were placed 50.8 mm apart. To put the MWNT-PVDF films in compression, the specimen was placed in the fixture with the film on the top face, as shown in Fig. 5. To apply tensile strain, the specimens were placed in the fixture with the film facing down. The load frame (Satec 22EMF, Instron) was displacement-controlled at a rate of $5 \text{ mm} \cdot \text{min}^{-1}$. The displacement was measured using a deflectometer (Epsilon 3540) connected to the load frame and placed at the center of the span. The films were subjected to tensile strains from 0 to $5,000 \mu\epsilon$ (in $1,000 \mu\epsilon$ increments) and then subjected to compressive strain, at the same amplitudes. At each strain step, an EIT measurement was taken, while the load frame

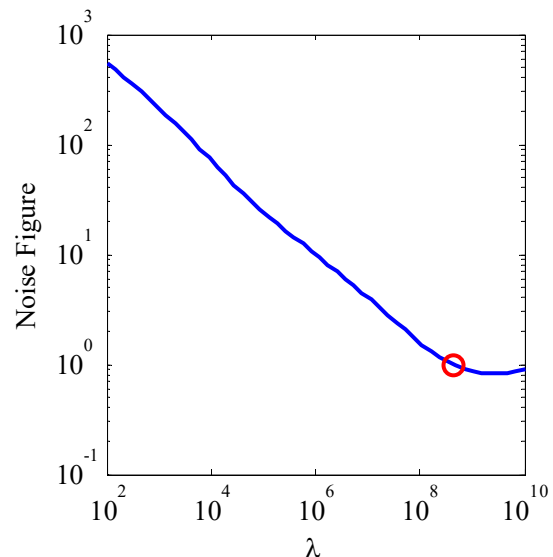


Fig. 6 Regularization plot with the hyperparameter (4.54×10^8) circled in red, corresponding to a noise figure of 1.

was paused. After all of the EIT measurements were taken, they were reconstructed with respect to the initial unstrained EIT measurement.

IV. RESULTS AND DISCUSSION

A. EIT Validation

1) Regularization Hyperparameter Determination

As stated previously, the regularization parameter is determined using a contrast between a homogeneous film and one with a small area in the center with a 50% decrease in conductivity. In this case, a 6 mm square at the center of a film was masked to act as the contrast area. The film resembled the specimen in Fig. 4, except only the center square was masked. To determine the appropriate regularization hyperparameter, the reconstruction algorithm was run for a range of hyperparameters logarithmically spaced between 10^2 and 10^{10} . For each reconstruction, the noise figure was calculated, and the responses are plotted in Fig. 6. The hyperparameter that corresponds to a noise figure of 1 is labeled with a red circle, and its value is 4.54×10^8 . The reconstruction that corresponds to this hyperparameter is shown in Fig. 7, where the contrast in the center can be easily seen.

2) EIT Reconstruction

Using the regularization parameter reported previously, all of the validation specimens were reconstructed in reference to the homogeneous MWNT-PVDF film specimen. These reconstructions took approximately 1 s each. The resulting reconstruction for the specimens with a masked cross in the center is shown in Fig. 8. The first point regarding this figure is the non-zero background. Because this reconstruction is a contrast between the homogeneous specimen and that with the masked cross, the non-masked areas will still not have the same conductivity background, due to the non-uniform method of spray-deposition by hand. However, the conductivity distribution taken using the four-point probe

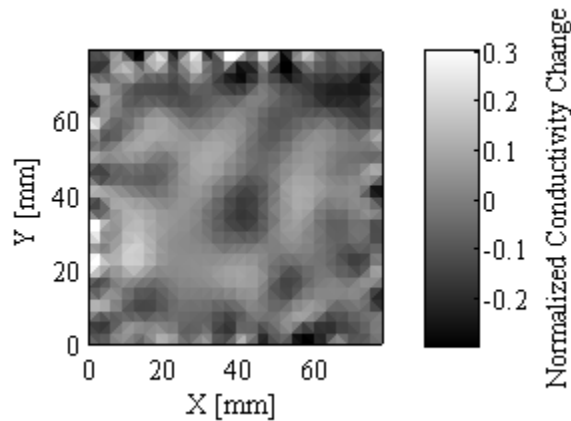


Fig. 7 EIT reconstruction for 6 mm center contrast corresponding to the hyperparameter with a noise figure of 1.

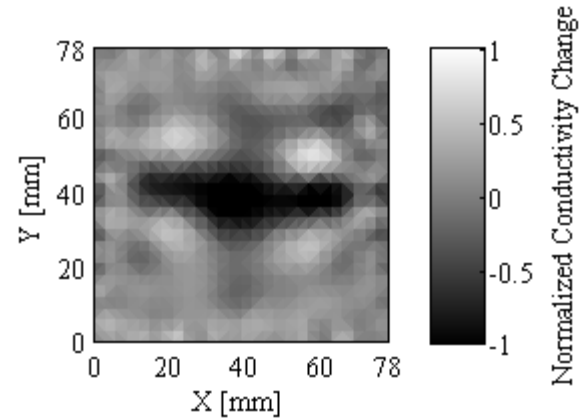


Fig. 8 The EIT reconstruction for the conductivity distribution with a 6 mm-wide cross contrast in the center of the sensing area.

measurements is shown in Fig. 9 and generally verifies the conductivity pattern reconstructed by the EIT method. In Fig. 9, there is a line of conductivity decrease in the top right side at a y coordinate of about 60 mm. This is presumably due to an effect of the spray deposition as the sprayer was swept in a horizontal direction across the substrates. The same decrease in conductivity is captured in the reconstruction. In addition, there are four areas of increased conductivity change in the EIT reconstruction that are not present in the actual conductivity distribution map. These are most possibly due to an effect that occurs with all EIT reconstructions, especially with sharp contrasts as in these specimens. A small region of opposite conductivity change will bound an area of actual contrast with a much lower magnitude. This small artifact is present in all reconstructions done for this study and is also observed in other studies [50, 64]. In the case of the cross contrast reconstruction, it is thought that this effect becomes exaggerated within the internal corners of the cross. Finally, the horizontal part of the cross is better resolved than the vertical portion of the cross. This is thought to be due to effects of the high-pass filter with the triangular mesh as opposed to a square mesh. In the previously reviewed work, the example reconstructions are always of round or square contrasts, so it is not known if these effects are present in those reconstruction approaches as well. However, despite these aspects of the reconstruction, this EIT approach is highly capable of capturing the complex shape of the cross contrast, as well as other smaller contrasts, like the 6 mm contrast used for determining the hyperparameter.

B. EIT Strain Response

Prior to discussing the EIT strain sensitivity, the piezoresistivity of the films is examined from the two-point probe resistance measurements, as a point of comparison. To facilitate a more straightforward comparison, the resistance

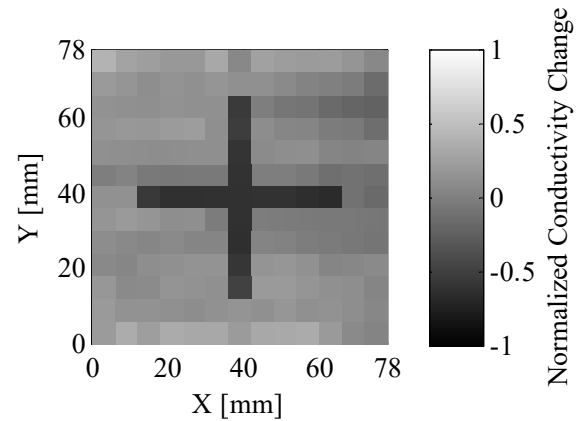


Fig. 9 A measured conductivity distribution using four-point probe measurements for the specimen with a 6 mm cross contrast.

measurements were converted to conductance using:

$$G = \frac{1}{R} \quad (7)$$

Furthermore, the percent change of the conductance was calculated for each strain value using:

$$\Delta G = \frac{G - G_0}{G_0} \times 100 \quad (8)$$

These corresponding measurements are plotted as a function of strain in Fig. 10. The main plot is the low-strain response from 0 to 5,000 $\mu\epsilon$, which are the same tensile strain levels that the EIT measurements were subjected to. The full strain conductance strain response is presented in the inset plot.

As illustrated in the inset plot in Fig. 10, the strain responses of the MWNT-PVDF films are bi-functional, with the lower strain response being linear until 4,000 $\mu\epsilon$. The

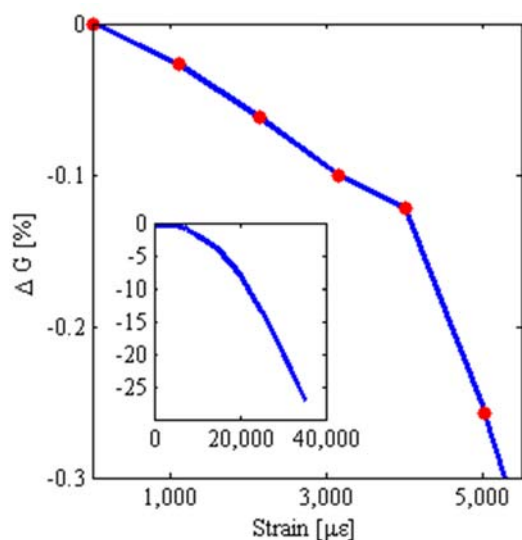


Fig. 10 The two-point conductance response of the MWNT-PVDF film to applied strain over the strain regime, from which the EIT measurements were taken. The inset plot is the full strain response of the two-point conductance measurements and has the same axes as the larger plot.

calculated linear gauge factor of these films is -0.481 ± 0.163 . At $4,000 \mu\epsilon$, the response becomes non-linear, which has been seen previously [40, 41, 70] as an indication that the film is undergoing cracking. To validate this, surface SEM images were taken of a tested film. A representative SEM image is presented in Fig. 11. From the image, one can see that the underlying substrate has cracked, leading to a tear in the film. However, a full characterization of this conductance strain response is out of the scope of the present text and is reserved for the future.

To determine if the MAP reconstruction scheme is sufficiently sensitive to perform SHM, the MWNT-PVDF films were subjected to low-level tensile and compressive strains. The corresponding EIT measurements were reconstructed in reference to the initial unstrained EIT measurements for each test. The hyperparameter was determined using the methodology laid out previously, using a 2 mm square contrast at the center of an $18 \times 18 \text{ mm}^2$ sensing area. From the mechanical tests, a representative reconstruction response is shown in Fig. 12. The center of the reconstructed conductivity distribution is relatively similar, but deviations can be seen near the boundaries of the reconstruction. This is partially due to the effects by strain on the electrodes that changes the contact resistance. This can have a significant effect on the reconstruction, but in this case these effects are relatively minor.

To characterize the MWNT-PVDF conductivity strain response using the EIT method, the median value of the conductivity distribution is calculated for each strain state. The median is used as opposed to the mean, due to the increased robustness of the calculation to outliers, which can occur near the boundaries. This is then plotted as a function of strain as shown in Fig. 13. As illustrated, the strain response is linear from approximately $-5,000 \mu\epsilon$ to $4,000 \mu\epsilon$. Within this linear

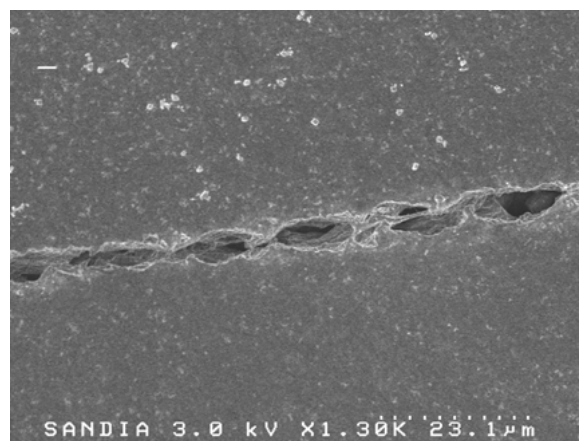


Fig. 11 An SEM image of a tear in the MWNT-PVDF film deposited on a GFRP substrate loaded in tension.

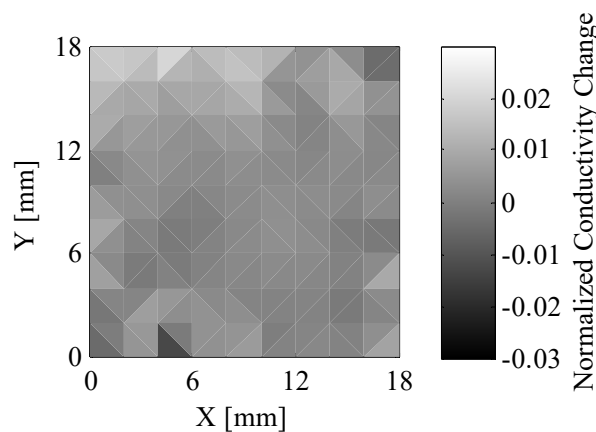


Fig. 12 An EIT reconstruction for a MWNT-PVDF film subjected to $3,000 \mu\epsilon$.

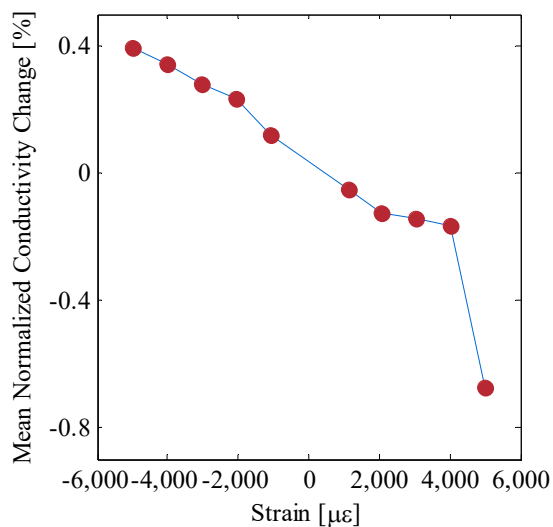


Fig. 13 The strain response as measured using the median value of the reconstructed conductivity distributions for a range of compressive and tensile strain values.

region, the gauge factor is calculated as -0.55 . This closely compares to the strain sensitivity calculated for the two-point

probe responses to lower values of applied strain. After 4,000 $\mu\epsilon$, a non-linear response is observed, as is consistent with the two-point conductance measurements discussed previously.

V. CONCLUSION

In this study, spatially distributed sensing was performed using a spray-deposited MWNT-PVDF film and electrical impedance tomography. The latex-based MWNT-PVDF film enabled the capacity for sensing over much larger areas than was previously demonstrated. In addition, the application of the linear reconstruction method called Maximum a Posteriori was discussed and characterized for detection of changes in conductivity distributions of MWNT-PVDF films when applied to the surface of GFRP composites. First, the capability of the algorithm was demonstrated by reconstructing the difference in spatial conductivity between a homogeneous conductivity map and one with a tailored conductivity distribution (*i.e.*, formed by masking and selectively depositing film in an area during spray fabrication). Finally, the MAP algorithm's sensitivity to small changes in conductivity due to applied strain to the MWNT-PVDF films was characterized. This sensitivity was compared to that measured by two-point conductance measurements and was proven to be as effective. In addition to the spatial sensitivity, the MAP algorithm facilitated faster reconstruction times than previously demonstrated for SHM purposes, enabling real-time sensing using EIT. This work provides a further step towards facilitating a paradigm shift in SHM by demonstrating the ability to perform spatially distributed sensing using piezoresistive thin films coupled with an electrical impedance tomography algorithm.

ACKNOWLEDGMENT

The authors thank Marianne LaFord and Roger Watson at Sandia National Laboratories for their input and help with the MWNT-PVDF formulation and mechanical testing, respectively.

REFERENCES

- [1] American Society of Civil Engineers, *2009 Report Card for America's Infrastructure*, 2009.
- [2] P. Knudson, "NTSB Continues Investigation of Southwest Airlines Flight 812", National Transportation Safety Board, ed., 2011.
- [3] M. V. Rosenker, "Safety Recommendation A-06-27 and -28", National Transportation Safety Board, ed., 2006.
- [4] C. P. Cavas, "Cracks plague Ticonderoga-class cruisers", *The Navy Times*, Gannett Government Media Company, 2010.
- [5] S. Ritchey, N. Adler, and M. Pischel, "Crack Monitoring Survey During Rough Water Trials Period #2", Naval Surface Warfare Center - Carderock, ed., 2011.
- [6] M. A. Rumsey, and J. A. Paquette, "Structural Health Monitoring of Wind Turbine Blades", in *SPIE Smart Structures / NDE*, San Diego, CA, USA, 2008, SPIE-2008-6933-14.
- [7] D. Barke, and K. W. Chiu, "Structural health monitoring in the railway industry: a review", *Structural Health Monitoring*, vol. 4, no. 1, pp. 81-94, 2005.
- [8] S. R. Hunt, and I. G. Hebden, "Validation of the Eurofighter Typhoon structural health and usage monitoring system", *Smart Materials and Structures*, vol. 10, no. 3, pp. 497, 2001.
- [9] H. Choi, S. Choi, and H. Cha, "Structural Health Monitoring system based on strain gauge enabled wireless sensor nodes", In *INSS 2008 - 5th International Conference on Networked Sensing Systems*, pp. 211-214.
- [10] D. Betz, L. Staudigel, and M. N. Trutzel, "Test of a fiber Bragg grating sensor network for commercial aircraft structures", *Optical Fiber Sensors Conference Technical Digest*, pp. 55-58 vol.1, 2002.
- [11] A. Cusano, P. Capoluongo, S. Campopiano, A. Cutolo, M. Giordano, F. Felli, A. Paolozzi, M. Caponero, "Experimental modal analysis of an aircraft model wing by embedded fiber Bragg grating sensors", *IEEE Sensors Journal*, vol. 6, no. 1, pp. 67-77, 2006.
- [12] H. Sohn, C. Farrar, N. Hunter, K. Worden, *Applying the LANL Statistical Pattern Recognition Paradigm for Structural Health Monitoring to Data from a Surface-Effect Fast Patrol Boat*, Los Alamos National Laboratory Report LA-13761-MS, Los Alamos National Laboratory, 2001.
- [13] W. Ecke, I. Latka, R. Willsch, A. Reutlinger, R. Graue, "Fibre optic sensor network for spacecraft health monitoring", *Measurement Science and Technology*, vol. 12, no. 7, pp. 974, 2001.
- [14] X. Chang, X. He, J. Hu, J. Li "Experimental Research on Embedded Fiber Bragg Grating Sensors Network for Solid Rocket Motors Health Monitor", In *First International Workshop on Intelligent Networks and Intelligent Systems*, Wuhan, China, 2008, pp. 170-173.
- [15] H.-N. Li, D.-S. Li, and G.-B. Song, "Recent applications of fiber optic sensors to health monitoring in civil engineering", *Engineering Structures*, vol. 26, no. 11, pp. 1647-1657, 2004.
- [16] R. C. Tennyson, A. A. Mufti, S. Rizkalla, G. Tadros, B. Benmokrane, "Structural health monitoring of innovative bridges in Canada with fiber optic sensors", *Smart Materials and Structures*, vol. 10, no. 3, pp. 560, 2001.
- [17] Z. Zhi, and J. Ou, "Development of FBG Sensors for Structural Health Monitoring in Civil Infrastructures Sensing Issues in Civil Structural Health Monitoring", F. Ansari, ed., pp. 197-207: Springer Netherlands, 2005.
- [18] J.-B. Ihn, and F.-K. Chang, "Pitch-catch active sensing methods in structural health monitoring for aircraft structures", *Structural Health Monitoring*, vol. 7, no. 1, pp. 5-19, 2008.
- [19] S. S. Kessler, E. B. Flynn, and M. D. Todd, "Hybrid Coherent/Incoherent Beam Forming Diagnostic Approach to Naval Assets", *Proceedings of the 8th International Workshop on Structural Health Monitoring*, vol. 2, pp. 1839-1846, 2011.
- [20] A. Gunasekaran, S. Cross, N. Patel, and S. Sedigh, "Recent enhancements to and applications of the SmartBrick structural health monitoring platform", In *SPIE Smart Structures and Materials and Nondestructive Evaluation and Health Monitoring*, San Diego, CA, pp. 83450S, 2012.
- [21] J. Wu, S. Yuan, S. Ji, G. Zhou, Y. Wang, and Z. Wang, "Multi-agent system design and evaluation for collaborative wireless sensor network in large structure health monitoring", *Expert Systems with Applications*, vol. 37, no. 3, pp. 2028-2036, 2010.
- [22] T. Hay, S. Jayaraman, A. Ledeczki, P. Volgyesi, R. Hay, "Railway Bridge Structural Health Monitoring Using Wireless Acoustic Emission Sensor Network", In *ASME/IEEE Joint Rail Conference*, JRC2009, Pueblo, CO, p. 57061, 2009.
- [23] J. Yun, "Development of Structural Health Monitoring Systems Incorporating Acoustic Emission Detection for Spacecraft and Wind Turbine Blades", M.S. thesis, Electrical and Computer Engineering, Virginia Tech, 2011.
- [24] A. Zagrai, D. Doyle, V. Gigineishvili, J. Brown, H. Gardenier, and B. Arritt, "Piezoelectric Wafer Active Sensor Structural Health Monitoring of Space Structures", *Journal of Intelligent Material Systems and Structures*, vol. 21, no. 9, pp. 921-940, 2010.
- [25] K. Ogi, "A Model for Piezoresistance Behavior in a CFRP Cross-Ply Laminate with Transverse Cracking", *Journal of Solid Mechanics and Materials Engineering*, vol. 1, no. 8, pp. 975-985, 2007.
- [26] M. Taya, W. J. Kim, and K. Ono, "Piezoresistivity of a short fiber/elastomer matrix composite", *Mechanics of Materials*, vol. 28, no. 1-4, pp. 53-59, 1998.
- [27] A. Todoroki, and J. Yoshida, "Electrical Resistance Change of Unidirectional CFRP Due to Applied Load", *JSME International Journal Series A: Solid Mechanics and Material Engineering*, vol. 47, no. 3, pp. 357-364, 2004.

- [28] S. Wang, and D. D. L. Chung, "Piezoresistivity in continuous carbon fiber polymer-matrix composite", *Polymer Composites*, vol. 21, no. 1, pp. 13-19, 2000.
- [29] S. Wang, and D. D. L. Chung, "Negative piezoresistivity in continuous carbon fiber epoxy-matrix composite", *Journal of Materials Science*, vol. 42, no. 13, pp. 4987-4995, 2007.
- [30] A. Todoroki, and M. Ueda, "Low-cost delamination monitoring of CFRP beams using electrical resistance changes with neural networks", *Smart Materials and Structures*, vol. 15, no. 4, pp. N75-N84, 2006.
- [31] A. Todoroki, "Delamination Monitoring Analysis of CFRP Structures using Multi-Probe Electrical Method", *Journal of Intelligent Material Systems and Structures*, vol. 19, no. 3, pp. 291-298, 2008.
- [32] A. Todoroki, H. Kobayashi, and K. Matuura, "Application of electric potential method to smart composite structures for detecting delamination", *JSMIE International Journal, Series A: Mechanics and Material Engineering*, vol. 38, no. 4, pp. 524-530, 1995.
- [33] H. Inoue, and K. Ogi, "Piezoresistance Behaviour of CFRP Cross-Ply Laminates with Transverse Cracking", *Key Engineering Materials*, vol. 334, no. 2, pp. 961-964, 2007.
- [34] L. Böger, M. H. G. Wichmann, L. O. Meyer, and K. Schulte, "Load and health monitoring in glass fibre reinforced composites with an electrically conductive nanocomposite epoxy matrix", *Composites Science and Technology*, vol. 68, no. 7-8, pp. 1886-1894, 2008.
- [35] I. Kang, M. J. Schulz, J. H. Kim, V. Shanov, and D. Shi, "A carbon nanotube strain sensor for structural health monitoring", *Smart Materials and Structures*, vol. 15, no. 3, pp. 737-748, 2006.
- [36] K. J. Loh, J. P. Lynch, B. S. Shim, N. A. Kotov, "Tailoring piezoresistive sensitivity of multilayer carbon nanotube composite strain sensors", *Journal of Intelligent Material Systems and Structures*, vol. 19, no. 7, pp. 747-764, 2008.
- [37] B. R. Loyola, V. La Saponara, and K. J. Loh, "Characterizing the self-sensing performance of carbon nanotube-enhanced fiber-reinforced polymers", SPIE Nondestructive Characterization for Composite Materials, Aerospace Engineering, Civil Infrastructure, and Homeland Security Conference, pp. 76490F-12, 2010.
- [38] M. D. Rein, O. Breuer, and H. D. Wagner, "Sensors and sensitivity: Carbon nanotube buckypaper films as strain sensing devices", *Composites Science and Technology*, vol. 71, no. 3, pp. 373-381, 2011.
- [39] S. M. Vemuru, R. Wahi, S. Nagarajaiah, and P. M. Ajayan, "Strain sensing using a multiwalled carbon nanotube film", *The Journal of Strain Analysis for Engineering Design*, vol. 44, no. 7, pp. 555-562, 2009.
- [40] L. Gao, E. T. Thostenson, Z. Zhang, and T.-W. Chou, "Coupled carbon nanotube network and acoustic emission monitoring for sensing of damage development in composites", *Carbon*, vol. 47, no. 5, pp. 1381-1388, 2009.
- [41] Y. Shindo, Y. Kuronuma, T. Takeda, Fumio, N., and S.-Y. Fu, "Electrical resistance change and crack behavior in carbon nanotube/polymer composites under tensile loading", *Composites Part B: Engineering*, pp. 39-43, 2011.
- [42] C. L. Cao, C. G. Hu, Y. F. Xiong, X. Y. Han, Y. Xi, and J. Miao, "Temperature dependent piezoresistive effect of multi-walled carbon nanotube films", *Diamond and Related Materials*, vol. 16, no. 2, pp. 388-392, 2007.
- [43] M. Shiraiishi, and M. Ata, "Conduction mechanisms in single-walled carbon nanotubes", *Synthetic Metals*, vol. 128, no. 3, pp. 235-239, 2002.
- [44] V. Skákalová, A. B. Kaiser, Y. S. Woo, and S. Roth, "Electronic transport in carbon nanotubes: From individual nanotubes to thin and thick networks", In *Advanced Semiconductor Devices and Microsystems International Conference, ASDAM 2006*, Smolenice, Slovakia, 2006.
- [45] B. S. Shim, W. Chen, C. Doty, C. Xu, and N. A. Kotov, "Smart electronic yarns and wearable fabrics for human biomonitoring made by carbon nanotube coating with polyelectrolytes", *Nano letters*, vol. 8, no. 12, pp. 4151-4157, 2008.
- [46] Q.-Y. Tang, Y. C. Chan, and K. Zhang, "Fast response resistive humidity sensitivity of polyimide/multiwall carbon nanotube composite films", *Sensors and Actuators B: Chemical*, vol. 152, no. 1, pp. 99-106, 2011.
- [47] H. Yu, T. Cao, L. Zhou, E. Gu, D. Yu, and D. Jiang, "Layer-by-Layer assembly and humidity sensitive behavior of poly(ethyleneimine)/multiwall carbon nanotube composite films", *Sensors and Actuators B: Chemical*, vol. 119, no. 2, pp. 512-515, 2006.
- [48] K. J. Loh, J. Kim, J. P. Lynch, N. W. S. Kam, and N. A. Kotov, "Multifunctional layer-by-layer carbon nanotube polyelectrolyte thin films for strain and corrosion sensing", *Smart Materials and Structures*, vol. 16, no. 2, pp. 429-438, 2007.
- [49] A. P. Calderon, "On an inverse boundary value problem," *Comp. Appl. Math*, vol. 25, no. 2-3, pp. 133-138, 2006 (reprinted from a 1980 conference paper of the Brazilian Mathematical Society, pp. 65-73)
- [50] A. Adler, and R. Guardo, "Electrical impedance tomography: regularized imaging and contrast detection", *IEEE Transactions on Medical Imaging*, vol. 15, no. 2, pp. 170-179, 1996.
- [51] W. R. Breckon, "Image reconstruction in electrical impedance tomography", Ph.D. dissertation, School of Computing and Mathematical Sciences, Oxford Polytechnic, United Kingdom, 1990, available under <http://eprints.ma.man.ac.uk/1083/>.
- [52] M. Cheney, D. Isaacson, J. C. Newell, S. Simske, and J. Goble, "NOSER: An algorithm for solving the inverse conductivity problem", *International Journal of Imaging Systems and Technology*, vol. 2, no. 2, pp. 66-75, 1990.
- [53] N. Polydorides, W. R. B. Lionheart, and H. McCann, "Krylov subspace iterative techniques: on the detection of brain activity with electrical impedance tomography", *IEEE Transactions on Medical Imaging*, vol. 21, no. 6, pp. 596-603, 2002.
- [54] T. J. Yorkey, J. G. Webster, and W. J. Tompkins, "Comparing reconstruction algorithms for electrical impedance tomography", *IEEE Transactions on Biomedical Engineering*, vol. BME-34, no. 11, pp. 843-852, 1987.
- [55] L. Horesh, M. Schweiger, S. Arridge, and D. Holder, "Large-scale non-linear 3D reconstruction algorithms for electrical impedance tomography of the human head", In *World Congress on Medical Physics and Biomedical Engineering Conference*, Seoul, Korea 2006, pp. 3862-3865, 2007.
- [56] N. Polydorides, "Image Reconstruction Algorithms For Soft-Field Tomography", Ph.D. dissertation, Department of Electrical Engineering and Electronics, University of Manchester Institute of Science and Technology, Manchester, United Kingdom, 2002.
- [57] M. Soleimani, and W. R. B. Lionheart, "Nonlinear image reconstruction for electrical capacitance tomography using experimental data", *Measurement Science and Technology*, vol. 16, pp. 1987, 2005.
- [58] EIDORS Collaboration, "Electrical Impedance Tomography and Diffuse Optical Tomography Reconstruction Software," 2011, available under <http://eidors3d.sourceforge.net/>
- [59] R. Lazarovitch, D. Rittel, and I. Bucher, "Experimental crack identification using electrical impedance tomography", *NDT and E International*, vol. 35, no. 5, pp. 301-16, 2002.
- [60] S. Pyo, K. J. Loh, T.-C. Hou, E. Jarva, and J. P. Lynch, "A wireless impedance analyzer for automated tomographic mapping of a nanoengineered sensing skin", *Smart Structures and Systems*, vol. 8, no. 1, pp. 139-155, 2011.
- [61] T.-C. Hou, K. J. Loh, and J. Lynch, "Spatial conductivity mapping of carbon nanotube composite thin films by electrical impedance tomography for sensing applications", *Nanotechnology*, vol. 18, no. 31, pp. 315501, 2007.
- [62] K. J. Loh, T.-C. Hou, J. P. Lynch, and N. A. Kotov, "Carbon Nanotube Sensing Skins for Spatial Strain and Impact Damage Identification", *Journal of Nondestructive Evaluation*, vol. 28, no. 1, pp. 9-25, 2009.
- [63] K. Paulson, W. Breckon, and M. Pidcock, "Electrode modelling in electrical impedance tomography", *SIAM Journal on Applied Mathematics*, vol. 52, no. 4, pp. 1012-1022, 1992.
- [64] B. M. Graham, and A. Adler, "Objective selection of hyperparameter for EIT", *Physiological measurements*, vol. 27, no. 5, pp. S65-S79, 2006.
- [65] A. N. Tikhonov, A. Goncharsky, V. V. Stepanov, and A. G. Yagola, *Numerical Methods for the Solution of Ill-Posed Problems*, Boston: Kluwer Academic Publishers, 1995.
- [66] A. Adler, T. Dai, and W. R. B. Lionheart, "Temporal image reconstruction in electrical impedance tomography", *Physiological measurements*, vol. 28, pp. S11-S17, 2007.

- [67] M. J. O'Connell, P. Boul, L. M. Ericson, C. Huffman, Y. Wang, E. Haroz, C. Kuper, J. Tour, K. D. Ausman, R. E. Smalley, "Reversible water-solubilization of single-walled carbon nanotubes by polymer wrapping", *Chemical Physics Letters*, vol. 342, no. 3-4, pp. 265-271, 2001.
- [68] I. N. Mazov, V. L. Kuznetsov, S. I. Moseenkov, A. V. Ishchenko, A. I. Romanenko, O. B. Anikeeva, T. I. Buryakov, E. Yu Korovin, V. A. Zhuraviev, and V. I. Susiyaev, "Electrophysical and Electromagnetic Properties of Pure MWNTs and MWNT/PMMA Composite Materials Depending on Their Structure", *Fullerenes, Nanotubes, and Carbon Nanostructures*, vol. 18, no. 4-6, pp. 505-515, 2010.
- [69] ASTM International, "ASTM Standard D3039: Standard Test Method for Tensile Properties of Polymer Matrix Composite Materials", *ASTM Standard D3039*, 2008.
- [70] B. R. Loyola, V. La Saponara, and K. J. Loh, "In Situ Strain Monitoring of Fiber-Reinforced Polymers using Embedded Piezoresistive Nanocomposites", *Journal of Material Science*, vol. 45, no. 24, pp. 6786-6798, 2010.



Bryan R. Loyola received the B.S. degree in physics (2005), the M.S. degree in mechanical and aeronautical engineering (2012), and the Ph.D. degree in mechanical and aeronautical engineering (2012) from the University of California, Davis (USA). His doctoral dissertation work was done under the combined guidance of Prof. Valeria La

Saponara and Prof. Kenneth J. Loh.

Since graduation, Dr. Loyola has been employed by Sandia National Laboratories in Livermore, CA (USA), as a Senior Member of the Technical Staff. His research interests include sensor development for structural health monitoring, spatially distributed measurement techniques, carbon nanotube thin film characterization, and electrospinning development and characterization.



Valeria La Saponara received a B.S. summa cum laude in aeronautical engineering (1994) from the University of Naples "Federico II" in Italy, and M.S. (1997) and Ph.D. (2001) degrees in aerospace engineering from the Georgia Institute of Technology (Atlanta, GA, USA).

In 1994-1996, she worked as a research fellow at the MARS Center, Italy, a subcontractor of NASA, the European Space Agency and the Italian Space Agency. After receiving her Ph.D. degree, she was an instructor in Civil and Environmental Engineering at Georgia Tech for one year, and an assistant professor in mechanical engineering at the University of Utah (Salt Lake City, UT, USA) for three years. In July 2005, she joined the faculty of the University of California, Davis (USA), and was promoted to associate professor with tenure in 2011. She is the director of the UC Davis Advanced Composites Research, Engineering and Science (ACRES) Laboratory. Her research interests are in the area of applied mechanics of fiber-reinforced polymer composite structures, with focus on durability improvements and structural health monitoring.

Dr. La Saponara received in 2007 a CAREER Award from the National Science Foundation (NSF). She is an active member of the American Society of Mechanical Engineers' Materials Division and Applied Mechanics Division.



Kenneth J. Loh (M'04) was born in Urbana, Illinois, in 1982. He received the B.S. degree in civil engineering from Johns Hopkins University (USA) in 2004. Thereafter, he received the M.S. degree in civil engineering in 2005, M.S. degree in materials science and engineering in 2008, and Ph.D. in civil engineering in 2008, all from the University of Michigan, Ann

Arbor (USA).

He is currently an assistant professor in the Department of Civil and Environmental Engineering at the University of California, Davis (since 2008). He is also the director of the Nano-Engineering and Smart Structures Technologies (NESST) Laboratory.

Dr. Loh's recent awards and honors include the Michigan Space Grant Consortium (MSGC) and NASA Fellowship in 2008, the SPIE Educational Scholarship in Optical Science and Engineering in 2008-2009, and the NSF CAREER Award in 2013. His research interests include bio-inspired sensors and actuators, multifunctional materials, thin films and nanocomposites, and structural health monitoring.



Timothy M. Briggs received the B.S., M.S., and Ph.D degrees in mechanical engineering from The University of Washington (USA) in 2005, 2006, and 2011, respectively. His research has focused on structural mechanics with an emphasis on composite materials.

Dr. Briggs is currently a staff member at Sandia National Laboratories (Livermore, CA, USA) where his responsibilities include research and development with a focus on advanced composite structures.



Greg O'Bryan was born in Whittier, California, in 1980. He received a B.S. in chemistry from the University of California Santa Cruz (USA) in 2002 and continued there to receive his Ph.D. in 2007 under the guidance of Prof. Rebecca Braslau in the field of controlled radical polymerization.

Starting as a postdoctoral researcher at Sandia National Laboratories (Livermore, CA, USA) in 2008, he has since remained employed at Sandia as a Senior Member of the Technical Staff.

Dr. O'Bryan has worked on mechanochromic stress sensing materials based on spiropyran moieties, percolation behavior in nanocomposites, and latex based coatings development. His research interests include smart coatings for self-cleaning

applications, nanocomposite materials for 3D printable device fabrication, polyhedral oligomeric silsesquioxane (POS) macroinitiators in controlled radical polymerizations, and redox chemistry of nitroxides for all organic thin film battery development.



Jack L. Skinner (M'07) received the B.S. degree from Montana Tech of the University of Montana, Butte, MT, in General Engineering with a Mechanical Engineering Option in 2000, the M.S. degree from Washington State University, (Pullman, WA, USA) in Mechanical Engineering in 2002, and the Ph.D. degree from the University of California, Davis,

CA (USA), in Mechanical Engineering in 2007.

He was a graduate researcher with the Berkeley Sensor and Actuator Center (BSAC), Berkeley, CA, from 2004 to 2007, where he developed diffractive optical microsystems. From 2003 to 2012, he was with Sandia National Laboratories, Livermore, CA, USA, where he was a Principal Member of the Technical Staff, before accepting a position as Assistant Professor of Mechanical Engineering in the General Engineering Department at Montana Tech, Butte, MT (USA). He has been working in the field of microelectromechanical systems (MEMS) and nanotechnology since 2001. His research interests include technological advancements in the understanding and application of microscale and nanoscale devices, materials, and methods, particularly to the area of energy.

Dr. Skinner is a member of the American Society of Mechanical Engineers (ASME), the Materials Research Society (MRS), the American Institute of Aeronautics and Astronautics (AIAA), and the American Society for Engineering Education (ASEE).